Materials Characterization 168 (2020) 110507

Contents lists available at ScienceDirect

Materials Characterization

journal homepage: www.elsevier.com/locate/matchar

Friction stir welding of 2060–T8 Al-Li alloy. Part II: Tensile fracture behavior

Y. Tao, Z. Zhang*, B.H. Yu, P. Xue, D.R. Ni, B.L. Xiao, Z.Y. Ma*

Institute of Metal Research, Chinese Academy of Sciences, Shenyang 110016, China

ARTICLE INFO

Keywords:
Friction stir welding
Aluminum–lithium alloys
Microstrucrure
Microtexture
Hardness
Fracture behavior

ABSTRACT

For friction stir welded (FSW) joints of conventional precipitation-hardened aluminum alloys, the lowest hardness zone (LHZ) was located at heat affected zone (HAZ) and determined the tensile fracture behavior with the fracture occurring at the LHZ. For FSW 2060–T8 joints, however, the LHZs were located at the nugget zone (NZ) under 400 rpm–200 mm/min, but at the HAZ under 800 rpm–200 mm/min, 1200 rpm–200 mm/min and 1200 rpm–50 mm/min. While the FSW 2060–T8 joints normally fractured along the LHZ under 400 rpm–200 mm/min and 1200 rpm–50 mm/min, abnormal fracture occurred at the thermo–mechanically affected zone (TMAZ) under 800 rpm–200 mm/min and 1200 rpm–200 mm/min. The FSW 2060–T8 joints with 800 rpm–200 mm/min and 1200 rpm–200 mm/min presented obvious diversity of crystal orientation and grain morphology, and subsequent deformation in the LHZs, the lower TMAZ and upper TMAZ. The large Schmid factor, coarse grains and δ′/β′ precipitates caused the preferential deformation and planar slip at the lower TMAZ, weakened the mechanical properties of the TMAZ, and therefore resulted in the abnormal failure at the TMAZ of FSW 2060–T8 joints under 800 rpm–200 mm/min and 1200 rpm–200 mm/min.

1. Introduction

Compared to the first and second generations [1–3], the third generation of Al-Li alloys exhibited remarkably improved mechanical properties and anisotropy by increasing the Cu content, reducing the Li content, and adding the Mg, Ag, Mn, and Zn elements, as well as adopting proper heat treatment. However, the third generation of Al-Li alloys still presented certain anisotropy of mechanical properties, but the reason was lack of detailed investigation [4].

The anisotropy of mechanical properties in the Al-Li alloys is generally believed to be related with the grain morphology and precipitates [2,4]. Thus, any variation in the grain morphologies and precipitates would affect the anisotropy. As mentioned in Part I [5], the FSW process resulted in the obviously different precipitate and grain evolutions in the nugget zone (NZ), thermo–mechanically affected zone (TMAZ) and heat affected zone (HAZ) of friction stir welded (FSW) 2060–T8 joints. This implies that the FSW joints of third generation of Al-Li alloys would exhibit severer anisotropy of mechanical properties compared to the base metal (BM).

For the FSW joints of conventional precipitation–hardened (2xxx, 6xxx, and 7xxx) aluminum alloys, the lowest hardness zone (LHZ) was generally located at the HAZ and determined the mechanical properties and fracture behavior of the FSW joints because the fracture occurred usually along the LHZs [6–8]. However, the fracture behavior of the FSW Al-Li alloy joints has unique characteristics.

The tensile fracture behavior of FSW joints of the third generation of Al-Li alloys has been reported in a number of studies [9–13]. Shukla et al. [9] reported that for 1 mm thick FSW 2195–T8 joints under 2200 rpm–150 mm/min and 2400 rpm–75 mm/min, the LHZ was located at the HAZ, but the FSW joints abnormally fractured at the NZ during tension. Chen et al. [10] inferred that the abnormal fracture at the NZ was related with the “S” line (originating from oxide film of the butting surfaces) for FSW 2A97 joints under rotation rates of 600–1200 rpm with a welding speed of 200 mm/min. Tao et al. [11] reported that 3.2 mm thick FSW 2198–T8 joints under 800 rpm–200 mm/min and 1600 rpm–200 mm/min showed the abnormal tensile fracture at the NZ, which was attributed to the low Taylor factor and lithium (Li) segregation at grain boundaries in the transition zone of the shoulder–affected zone (SDZ) and the pin–affected zone (PDZ).

2060–T8, a new third generation Al-Li alloy, has been subjected to FSW investigation recently. Mao et al. [12] reported that, for the FSW joints under rotation rates of 750–1500 rpm and welding speeds of 95–150 mm/min, the fracture locations were all consistent with the LHZs. Differently, Cai et al. [13] revealed that although the FSW joint under 2400 rpm–100 mm/min presented the LHZ at the HAZ, the FSW

* Corresponding authors.
E-mail addresses: zhangzhen@imr.ac.cn (Z. Zhang), zyma@imr.ac.cn (Z.Y. Ma).

https://doi.org/10.1016/j.matchar.2020.110507
Received 23 March 2020; Received in revised form 8 June 2020; Accepted 11 July 2020
Available online 15 July 2020

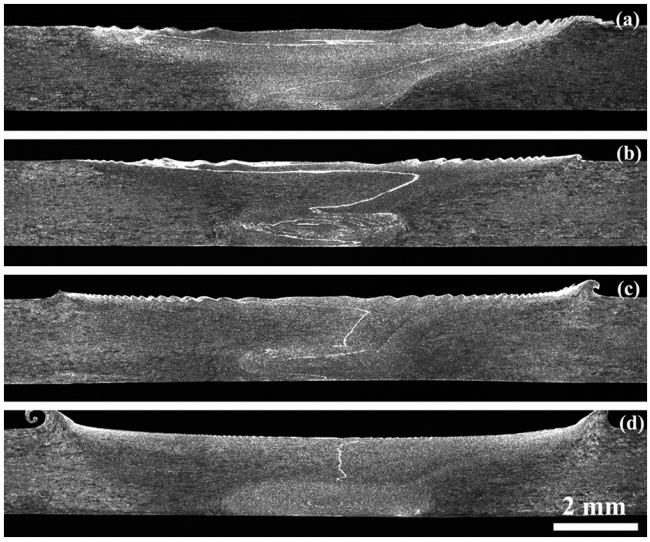

Fig. 1. Cross-sectional macroscopic patterns of "S" line of FSW 2060-T8 joints etched by 2% NaOH aqueous solution: (a) 400-200, (b) 800-200, (c) 1200-200 and (d) 1200-50.

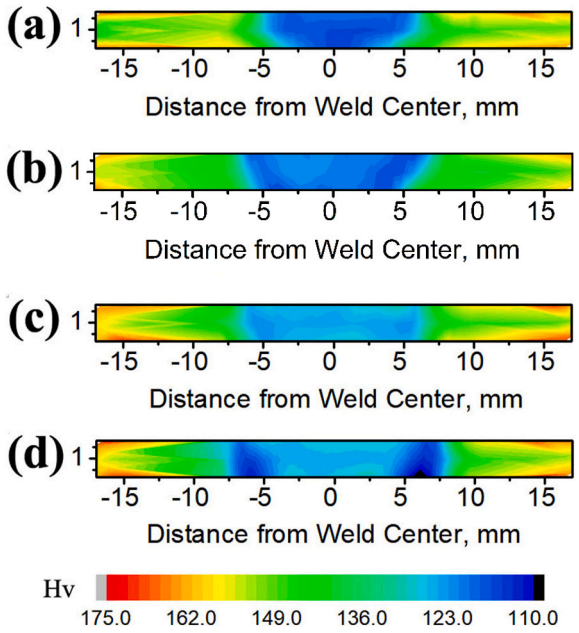

Fig. 2. Hardness contour maps of FSW 2060-T8 joints: (a) 400-200, (b) 800-200, (c) 1200-200 and (d) 1200-50.

joints fractured at the NZ/TMAZ interface. Liu et al. [14] found that the LHZ was located at the HAZ, but the fracture occurred at the NZ for the FSW joints under 800–1000 rpm with a welding speed of 300 mm/min. A similar phenomenon was observed in the FSW joints under 400–1300 rpm with a welding speed of 100 mm/min by Yan et al. [15] and under 800 rpm–200 mm/min for both natural and water cooling conditions by Ma et al. [16].

Clearly, different from that for conventional precipitation–hardened aluminum alloys, the inconsistency in the LHZ and fracture locations has been widely observed in the FSW joints for the Al-Li alloys. However, the exact origin for the abnormal failure of the FSW joints of the Al-Li alloys, in particular the third generation of Al-Li alloy 2060–T8 has not been reported so far.

Since thinning of the as–FSW joints was unavoidable, the varied cross–sectional areas at various locations of the joints undoubtedly would influence the fracture behavior of FSW 2060–T8 joints in previous studies [1,12–15]. With the help of joint surface planing, our study in Part I revealed that the grain microstructure and precipitate evolutions determined the hardness profiles and intrinsic mechanical properties of FSW 2060–T8 joints. It was unequivocally confirmed that the FSW 2060–T8 joints under both 800 rpm–200 mm/min and 1200 rpm–200 mm/min presented abnormal failure in the TMAZ although the LHZ was located at the HAZ. This needs an in–depth study to elucidate the origin for this abnormal phenomenon.

In this study, FSW 2060–T8 joints, prepared under various FSW parameters were subjected to the fracture investigation. The objective is to (a) reveal the intrinsic relationship between welding parameters and fracture location, (b) elucidate the exact factors resulting in the abnormal failure in the TMAZ instead of the LHZ for the FSW 2060–T8 joints.

2. Experimental procedure

The base material, FSW process and parameters, sample designation, naturally aging time, preparation of optical microscopic (OM) and transmission electron microscopic (TEM) specimens, and tensile tests have been described in detail in Part I.

The fracture morphologies of the FSW samples were examined by scanning electron microscopy (SEM, Quanta–600, FEI Company, Hillsboro, USA). To observe the distribution of the "S" line, the samples were etched using 2% NaOH aqueous solution and then washed with 20% nitric acid alcohol solution.

In order to obtain the hardness distribution maps, a total of three test lines were measured through the cross section at an interval of 0.7 mm, with a total of 93 indentations. In each line, there were 31 indentations that extended from the weld center to as far as 15 mm at an interval of 1 mm on both retreating side (RS) and advancing side (AS).

Crystallographic texture analysis of the welds was undertaken using electron backscattered diffraction (EBSD). Sample preparation consisted of grinding and mechanical polishing, followed by electro–-polishing using a solution of 30% nitric acid in methanol for 15 s at −25 °C and 12 V. Acquisition of the EBSD data was done using an FEI Sirion field–emission gun SEM equipped with a fully automatic HKL Technology EBSD attachment, operated at 20 kV. Data processing was then carried out using HKL Channel 5 software.

Time–of–flight secondary ion mass spectroscopy (TOF–SIMS) analysis was performed using an ION TOF–SIMS V in both negative and positive modes to reveal solute distribution in the NZ of the weld. TOF–SIMS samples were prepared through grinding, then mechanical polishing. Cesium ions were used for surface milling of the sample.

3. Results

3.1. Distribution of "S" line

The "S" line was a unique feature in the NZ for FSW aluminum alloy joints, originating from the oxide film on the initial butting surfaces, and was considered to influence the fracture behavior of FSW 2A97 joints [10]. In the FSW joint of aluminum alloys, the "S" line could be clearly observed under OM after etching with 2% NaOH aqueous solution [17]. Fig. 1 shows the cross–sectional macroscopic morphologies of samples 400–200, 800–200, 1200–200 and 1200–50. The "S" lines were clearly observed and the shape of "S" line was apparently affected by the welding parameters. The "S" line showed a zigzag pattern in sample 400–200 (Fig. 1a). When increasing the rotation rate from 400 to 800 rpm, the "S" line was discernible in the SDZ but was ambiguous in the PDZ in sample 800–200 (Fig. 1b). The pattern of the "S" line was essentially unchanged in sample 1200–200 with further increasing the rotation rate from 800 to 1200 rpm (Fig. 1c). At a constant rotation rate of 1200 rpm, decreasing the welding speed from 200 to 50 mm/min resulted in minor influence on the "S" line at the SDZ but near

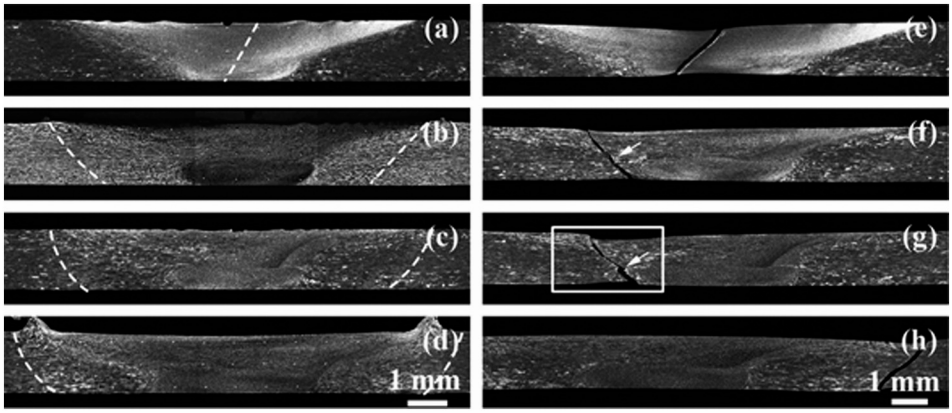

Fig. 3. Cross-sectional macroscopic morphologies of FSW 2060-T8 joints etched with Keller's reagent: (a) 400-200, (b) 800-200, (c) 1200-200, (d) 1200-50; and typical fracture location of samples: (e) 400-200, (f) 800-200, (g) 1200-200, (h) 1200-50.

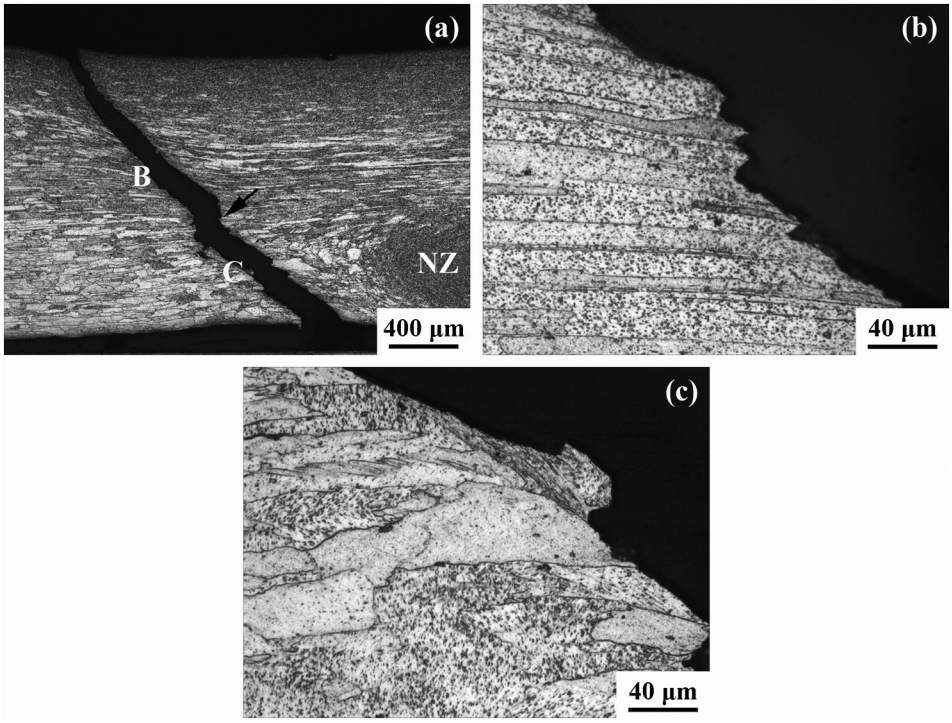

Fig. 4. Optical microstructure of failed sample 1200–200: (a) magnified micrograph of rectangular zone in Fig. 3g; further magnified micrographs of positions B and C in Fig. 4a: (b) position B, (c) position C.

disappearance of the "S" line at the PDZ in sample 1200–50 (Fig. 1d).

3.2. Microhardness map

Noted that the single hardness profile in Part I could not predict the fracture path of the FSW 2060–T8 joints because of the limited lowest hardness points. In order to accurately predict the fracture behavior of the FSW 2060–T8 joints, the microhardness contour maps of various FSW samples were measured and are shown in Fig. 2. For sample 400–200, a LHZ was discernible in the NZ (Fig. 2a). In contrast, two LHZs were obviously observed in the HAZ of samples 800–200 and 1200–200 and 1200–50 on both the RS and the AS (Fig. 2b–d), respectively.

3.3. Fracture location and morphology

Fig. 3 presents the cross–sectional macroscopic morphologies of samples 400–200, 800–200, 1200–200 and 1200–50, showing the locations of the LHZs (marked by the white dotted line in Fig. 3a–d) and the typical fracture locations (Fig. 3e–h). Generally, the fracture path was about 45° angle to the tension direction for the four samples. There are four important findings: (a) Sample 400–200 fractured at the NZ but not along the "S" line, indicating that the failure behavior of sample 400–200 was independent of "S" line (Fig. 3a and e); (b) Samples 800–200 and 1200–200 abnormally fractured at the TMAZ rather than the LHZ (HAZ) (Fig. 3b, c, f and g); (c) Sample 1200–50 fractured along the LHZ on the AS (Fig. 3d and h), which was in good agreement with the typical fracture locations of FSW joints of conventional

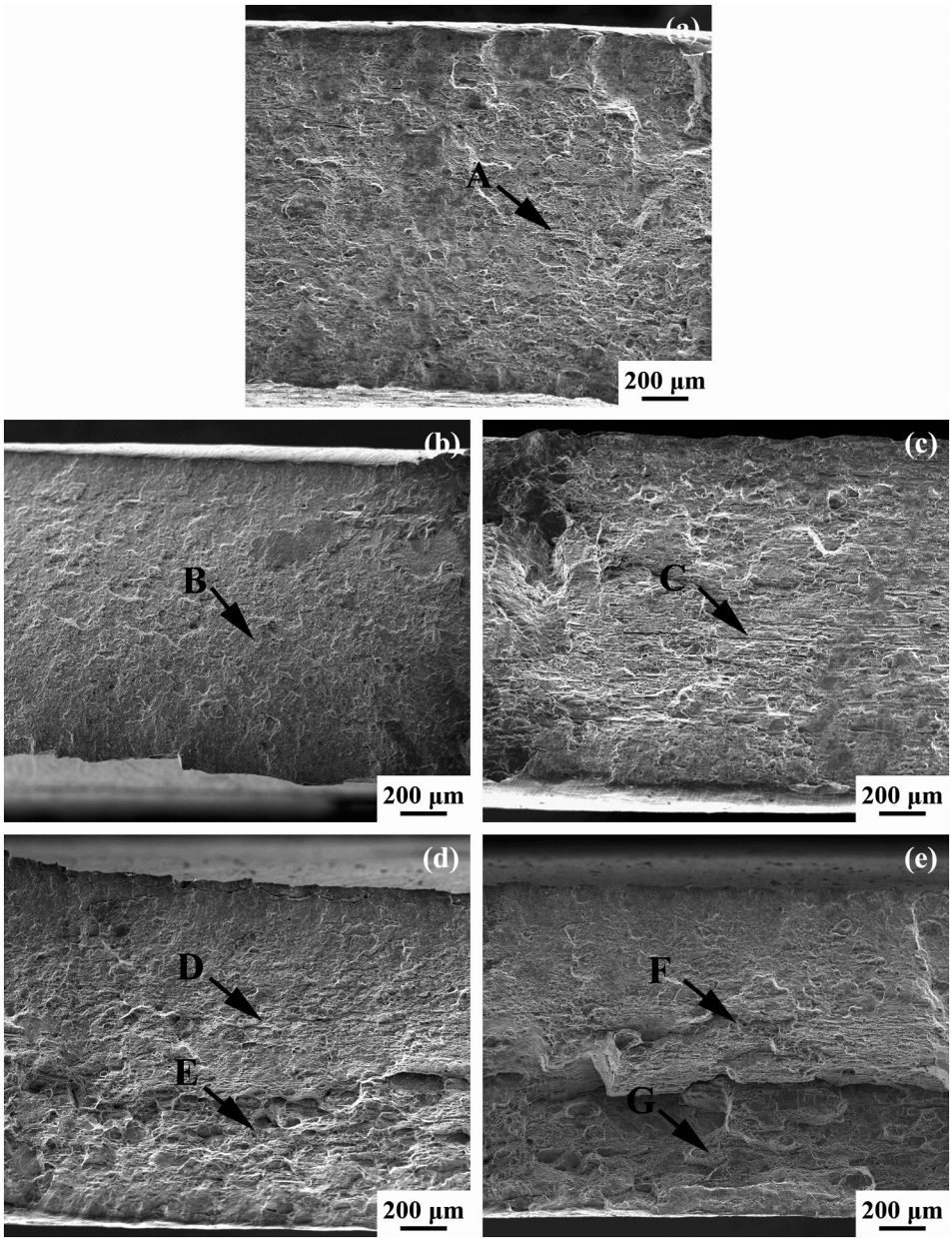

Fig. 5. Macrographic fractographs of FSW 2060-T8 joints: (a) BM; (b) 400-200, (c) 1200-50, (d) 800-200, and (e) 1200-200.

precipitation–hardened Al alloys [6,18,19]; (d) The fracture path was straight for samples 400–200 and 1200–50 (Fig. 3e and h) but was steps–like for samples 800–200 and 1200–200 (marked by arrows in Fig. 3f and g).

In order to make clear the reason of the abnormal fracture behavior, the magnified micrograph of the fracture path of sample 1200–200 (marked with a white box in Fig. 3g) is shown in Fig. 4. There was a transition step between the upper path and the lower path (marked by an arrow in Fig. 4a). The further magnified views of positions B and C in Fig. 4a indicated that the fracture path of sample 1200–200 was characterized by transgranular fracture at the upper TMAZ but showed mixed transgranular and intergranular fracture at the lower TMAZ (Fig. 4b and c). The fracture characteristics of sample 800–200 were similar to that of sample 1200-200 (not shown).

Figs. 5 and 6 show the typical SEM fractographs of the BM, samples 400–200, 800-200, 1200-200, and 1200–50 under different magnifications. The macroscopic images of the BM, samples 400–200 and 1200–50 showed the similar flat fracture surfaces but significant delamination was only observed in sample 1200–50 (Fig. 5a–c). The magnified images showed lots of large and deep dimples and few laminations along the rolling directing at position A of the BM (Fig. 6a), and mixed fracture with tiny dimples at position B for sample 400–200 (Fig. 6b). Compared with that of the BM, fewer dimples and much more delaminations were found at position C of sample 1200–50 (Fig. 6c). It is noted that the lamination phenomena corresponds to the delamination cracking as mentioned in Part I of this study. For samples 800-200 and 1200–200, the macroscopic image showed flat fracture surface at the upper TMAZ but uneven surface at the lower TMAZ (Fig. 5d and e);

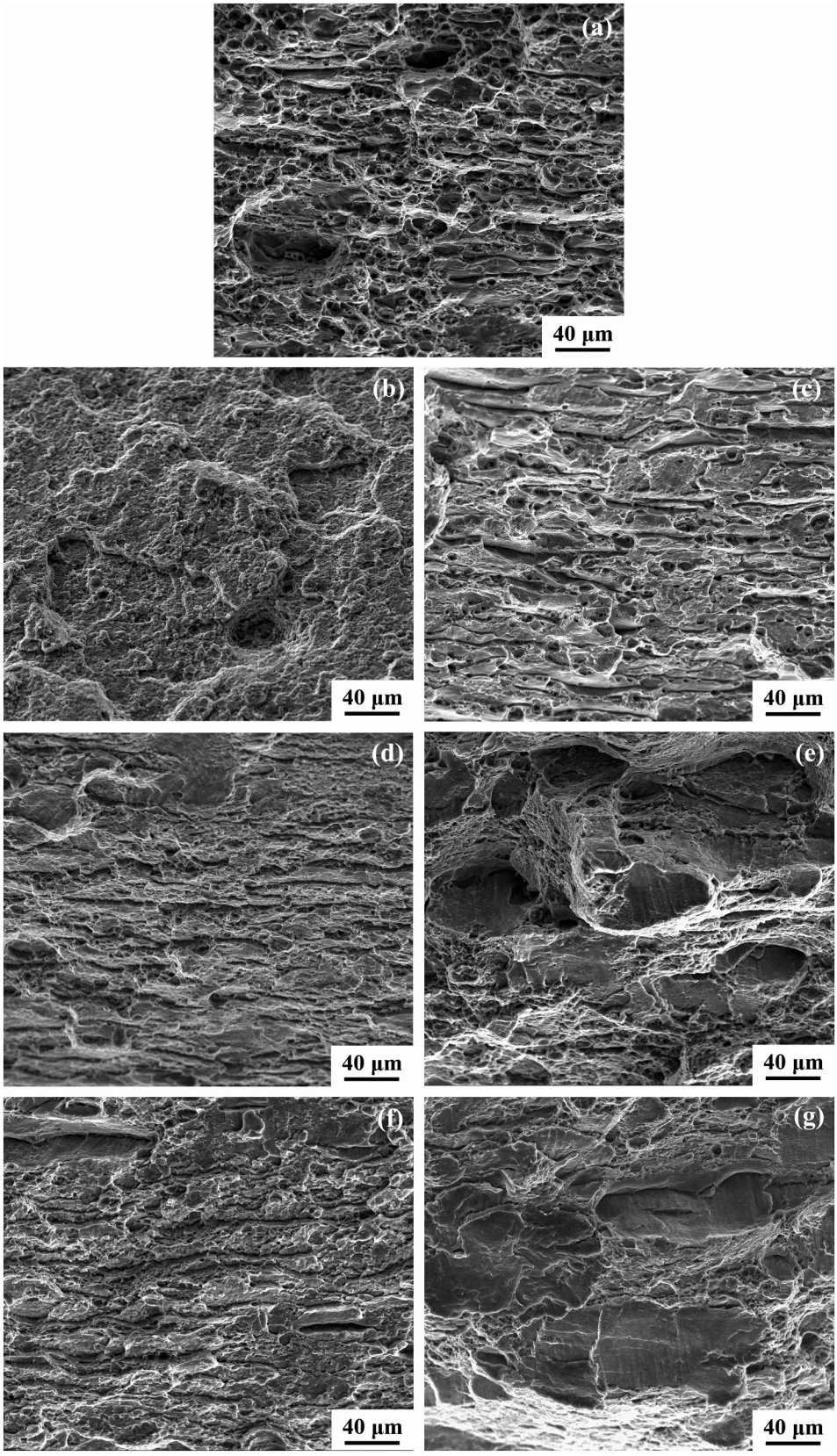

Fig. 6. Magnified micrographs of Fig. 5 from position A to position E: (a) position A, (b) position B, (c) position C, (d) position D, (e) position E, (f) position F and (g) position G.

Table 1
The locations of the lowest hardness zone (LHZ) and fracture of 2 mm FSW 2060-T8 joints with varied welding parameters and tools.

Rotation rate (rpm)	Welding speed (mm/min)	Should-pin diameter (mm)	Location of LHZ	Fracture location	Reference
800	200	10–4.5	HAZ	NZ	[1]
2400	100	7–1.8	HAZ	NZ/TMAZ interface	[12]
600–1000	300	10–4.2	NZ HAZ HAZ	NZ NZ NZ	[13]
750–1500	95–150	12–4	NZ or HAZ	NZ or HAZ	[14]
400–1300	100	12–4	HAZ	NZ	[15]
400 800 1200 1200	200 200 200 50	12–4	NZ HAZ HAZ HAZ	NZ TMAZ TMAZ HAZ	This study

the microscopic images showed the transgranular fracture at the upper positions D and F (Fig. 6d and f), and the mixture of intergranular and transgranular fracture at the lower positions E and G (Fig. 6e and g).

The above results indicated that samples 800–200 and 1200–200 exhibited the nearly identical abnormal failure at the TMAZ, so only sample 1200-200 was used for further observation and analysis.

4. Discussion

The LHZ and fracture locations of FSW 2060–T8 joints in Refs. 1, 12–15 and this study are summarized in Table 1. In the previous studies, two kinds of abnormal fracture locations, i.e., the NZ and NZ/TMAZ interface, were found for FSW 2060–T8 joints under the varied tools and welding parameters. It is noteworthy that these are not the intrinsic fracture locations for FSW 2060–T8 joints because of the varied cross–sectional areas at various locations of the as–FSW joints. By the joint surface planing, the FSW 2060–T8 joints exhibited an intrinsic abnormal fracture location of the TMAZ in this study. Thus, the intrinsic fracture behavior of FSW 2060–T8 joints can be analyzed in detail.

4.1. Abnormal fracture behavior of FSW 2060–T8 joints

The application of the first and second generation of Al-Li alloys was restricted by the strong tendency for intergranular fracture and high anisotropy of mechanical properties. In contrast, the third generation of Al-Li alloys presents the relatively weak intergranular fracture and anisotropic mechanical properties by adjusting the chemical compositions and heat treatments [20].

The factors affecting the intergranular fracture and anisotropic mechanical properties in Al-Li alloys have been reported previously by many investigators and different explanations have been put forward in those studies [21–28]. In general, several factors may affect the tensile deformation in the Al-Li alloys: (1) crystallographic texture; (2) presence of grain boundary precipitates, precipitate free zones (PFZs) or planar slip; (3) hydrogen, alkali–metal–impurity phase or Li segregation at the grain boundaries.

As mentioned above, the FSW process changed the microstructure in the NZ, TMAZ, and HAZ for the third generation of Al-Li alloys. It is highly possible that the above factors that led to the intergranular fracture and anisotropy of mechanical properties of the Al-Li alloys may affect the tensile fracture behavior of FSW Al-Li alloy joints. In this section, the above possible factors are discussed one by one to seek out

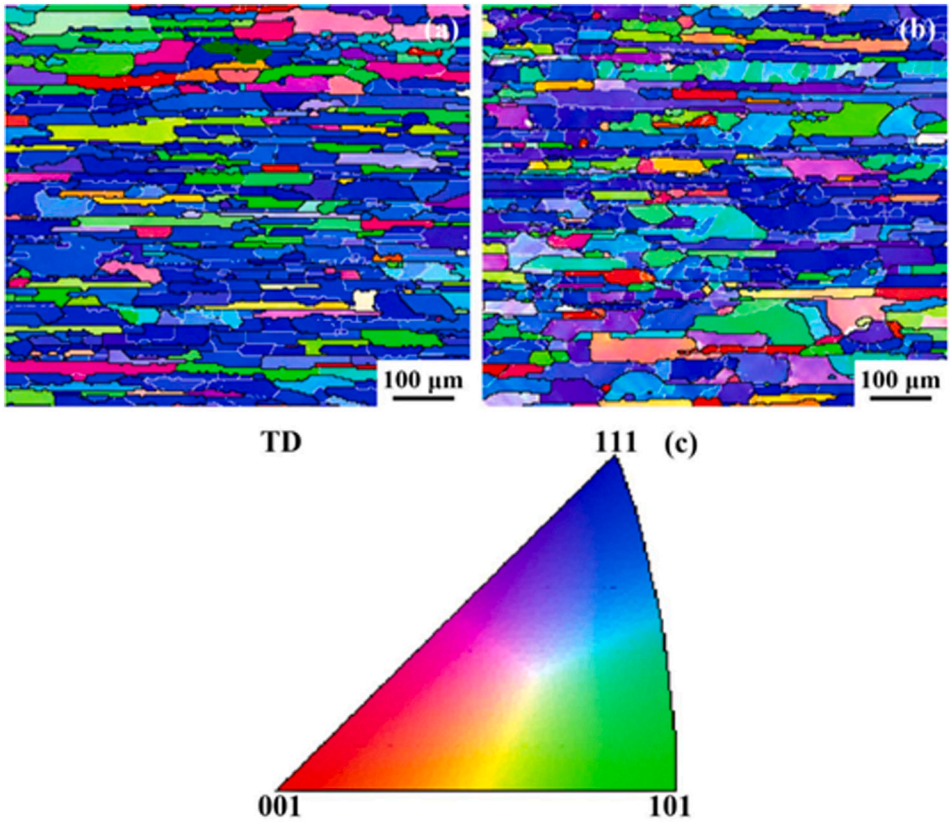

Fig. 7. Inverse pole figure colouring maps with respect to transverse direction for (a) BM, (b) LHZ of sample 1200-200, and (c) colouring triangle.

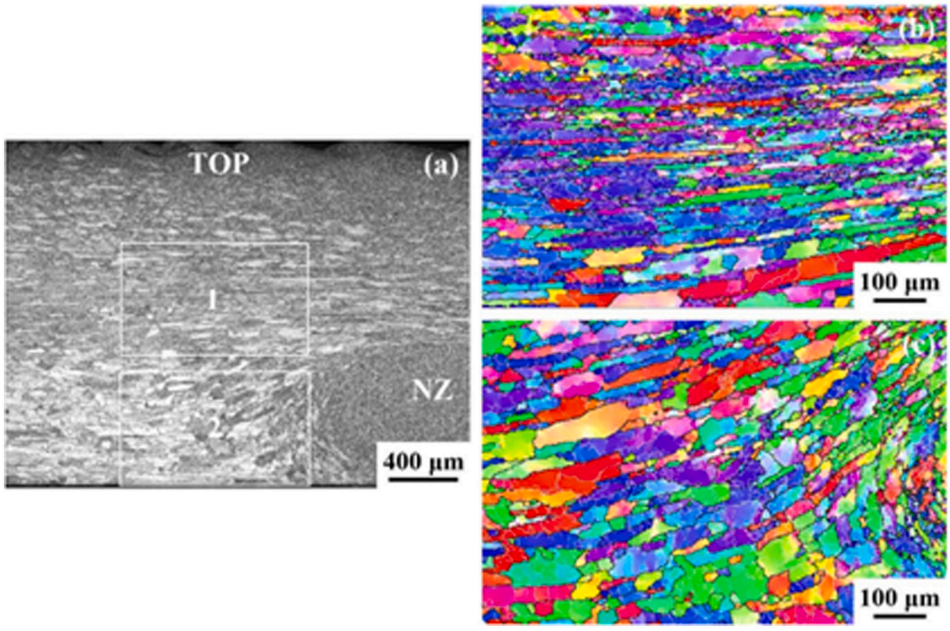

Fig. 8. (a) Optical microstructure of TMAZ of sample 1200-200; (b) and (c) inverse pole figure colouring maps with respect to transverse direction for rectangular areas 1-upper TMAZ and 2-lower TMAZ in Fig. 8a.

the exact reason for intergranular fracture in the TMAZ of sample 1200–200.

4.1.1. Crystallographic orientation

Fig. 7 shows the inverse pole figure colouring maps with respect to the transverse direction of the BM and LHZ of sample 1200–200. It shows that the ⟨111⟩ direction of most grains is parallel to the plate transverse (rolling direction) for the BM and the LHZ of sample 1200–200. Fig. 8 shows the inverse pole figure colouring maps with respect to the transverse direction of the TMAZ for sample 1200–200. It can be seen that the upper TMAZ exhibited elongated lath–shaped grains and ⟨111⟩ crystallographic texture, whereas coarse blocky–-shaped grains and random crystallographic orientation were observed in the lower TMAZ. These results were further verified by the inverse pole figures of the LHZ, upper and lower TMAZ of sample 1200–200 (Fig. 9).

The above results indicated that the crystallographic orientation varied in the LHZ, the upper and lower TMAZ for sample 1200–200. Thus, it can be inferred that the three regions might present different plastic deformation abilities, which are closely related with the crystal orientation of grains. Schmid factor, i.e., orientation factor, reflects the actual shear stress acting on the active slip surface along the slip direction and is the index for the plastic deformation ability of metal materials. Based on the EBSD analysis, the average Schmid factors of the LHZ, upper TMAZ and lower TMAZ were determined to be 0.41, 0.44 and 0.45, respectively. These results imply that the difficulty degree of plastic deformation during tension along the transverse direction is: LHZ > upper TMAZ > lower TMAZ. Therefore, the plastic deformation preferentially occurred at the lower TMAZ for sample 1200–200 during tension.

4.1.2. Presence of grain boundary precipitates, PFZs or planar slip

The presence of grain boundary precipitates and PFZs adjacent to the grain boundaries undoubtedly facilitated intergranular fracture in the AI–Li alloys, due to strain localization in the soft PFZs and nucleation of voids at the grain boundary precipitates [21]. Moreover, the Al-Li alloys were apt to planar slip when coherent δ′ precipitates were present as main strengthening precipitates because coherent δ′ precipitates were easily sheared by dislocations, thereby facilitating subsequent slip on the same slip plane [22]. Planar slip was the most often cited opinion for intergranular fracture in the Al-Li alloys. It was suggested that planar slip bands impinging upon the grain boundaries could produce local stress concentrations and therefore promoted intergranular fracture [23].

The TEM bright field micrographs of the lower TMAZ of failed sample 1200–200 are shown in Fig. 10. It can be seen that, in the lower TMAZ, no grain boundary precipitates and PFZs were observed (Fig. 10a), while lots of fine δ′/β′ precipitates were confirmed by the superlattice reflections in SAD pattern in ⟨100⟩ Al zone axis (Fig. 10b). Moreover, coarse planar slip bands were observed in the interior of the relatively big grains (Fig. 10c), indicating that the remarkable planar slip occurred in coarsened grains during tension. The two main reasons for this phenomenon are as follows. Firstly, the main strengthening precipitate was coherent δ′ precipitate, which was easily sheared by dislocations and thereby facilitated subsequent slip on the same slip plane. Secondly, Csontos et al. [22] reported that the grain size was proportional to the intensity of planar slip for Al–Li–Cu–X alloys. The coarse grains obviously facilitated the planar slip in the lower TMAZ.

4.1.3. Li, hydrogen or alkali–metal–impurity phase segregation at grain boundaries

Hydrogen segregation would undoubtedly weaken the mechanical properties of Al alloys. Absorption of hydrogen is inevitable for Al alloys because the Al melt contacted moisture in the atmosphere during melting. Especially, the Al-Li alloys contained higher levels of hydrogen than conventional Al alloys owing to the strong affinity between hydrogen and Li [24]. Sweet et al. [25] reported that liquid Na–K–rich phases (≥5–10 ppm) at the grain boundaries resulted in intergranular fracture for 2090 Al-Li alloy due to liquid–metal embrittlement. Moreover, Li segregation at the grain boundaries was believed to be

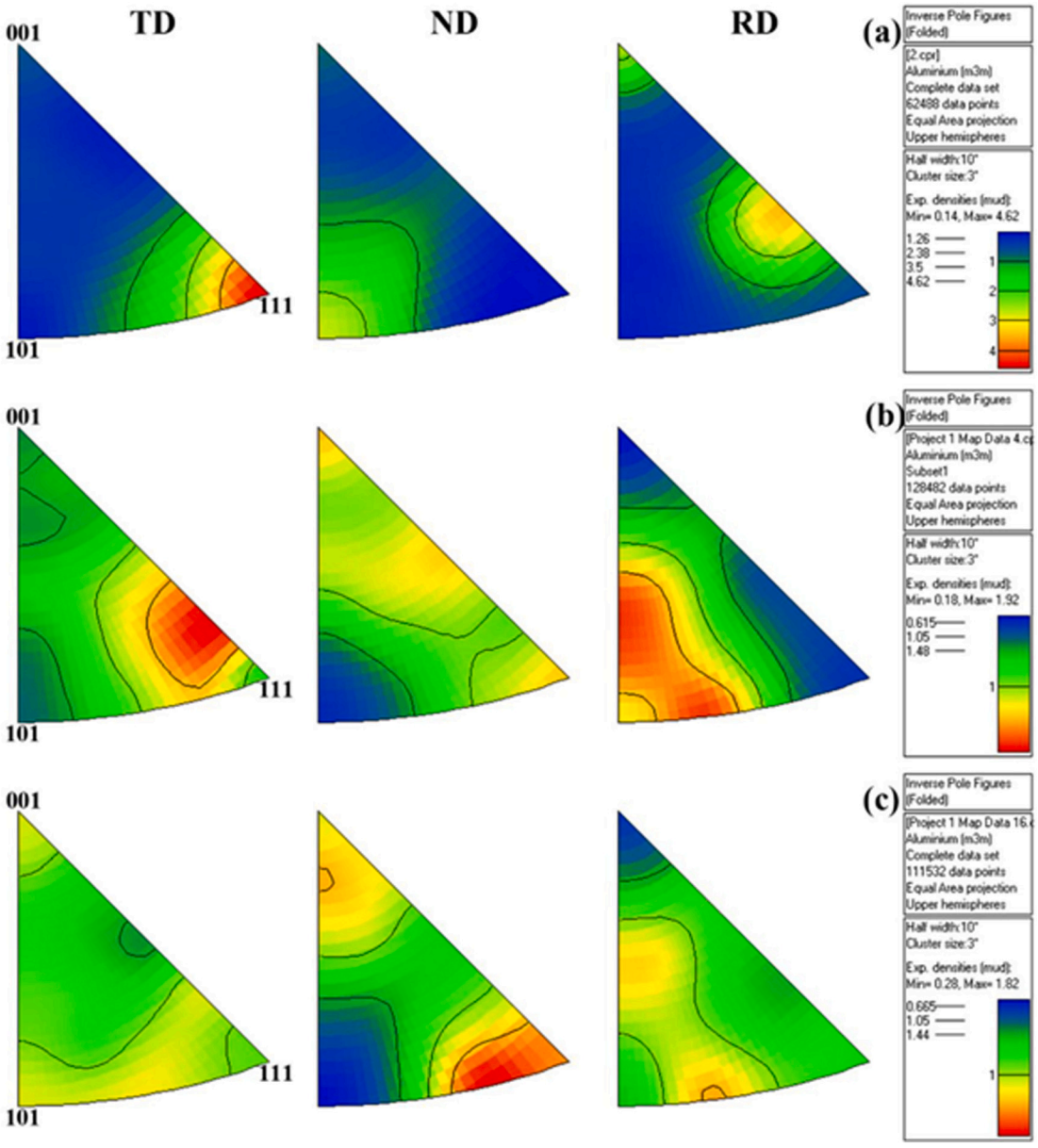

Fig. 9. Inverse pole figures of sample 1200-200: (a) LHZ, (b) upper TMAZ, and (c) lower TMAZ.

mainly responsible for intergranular fracture and low toughness in the Al-Li alloys [26–28].

In order to determine whether Li or hydrogen or alkali–metal–impurity phase segregation at the grain boundaries is the cause of intergranular fracture at the lower TMAZ of sample 1200–200, SIMS was used to analyze the solute atom distribution in this area. The distributions of Li, hydrogen and Na solute atoms (K solute atoms were not shown) in the BM, the NZ and the lower TMAZ of sample 1200–200 are shown in Fig. 11. It was shown that there was no Li, hydrogen or alkali–metal–impurity phase enrichment at the grain boundaries of the BM, the NZ and the lower TMAZ for sample 1200–200.

Based on these above results, it can be concluded that two main factors induced the abnormal fracture at the TMAZ for sample 1200–200. Firstly, compared with the LHZ and the upper TMAZ, the lower TMAZ exhibited a soft crystallographic orientation. Therefore, plastic deformation occurred preferentially at the lower TMAZ during tension. Secondly, the microstructure at the lower TMAZ was characterized by the coarse grains and δ′/β′ precipitates. When these coarse grains were under the tensile stress condition, a significant planar slip occurred. The coarse planar slip zones aggregated at the grain boundaries, caused the local high stress concentration and nucleation of microcracks at the grain boundaries [22,23], and eventually resulted in the intergranular and transgranular mixture fracture at the lower TMAZ of samples 800–200 and 1200–200 (Fig. 6e and g).

Compared with that of the lower TMAZ, the planar slip rarely occurred in the upper TMAZ for sample 1200–200 due to the finer and longer grains. So, the local stress concentration at the grain boundaries was insufficient to cause microcracks at the grain boundaries. Therefore, transgranular fracture was the primary mode of fracture in the upper TMAZ for samples 800–200 and 1200–200 (Fig. 6d and f).

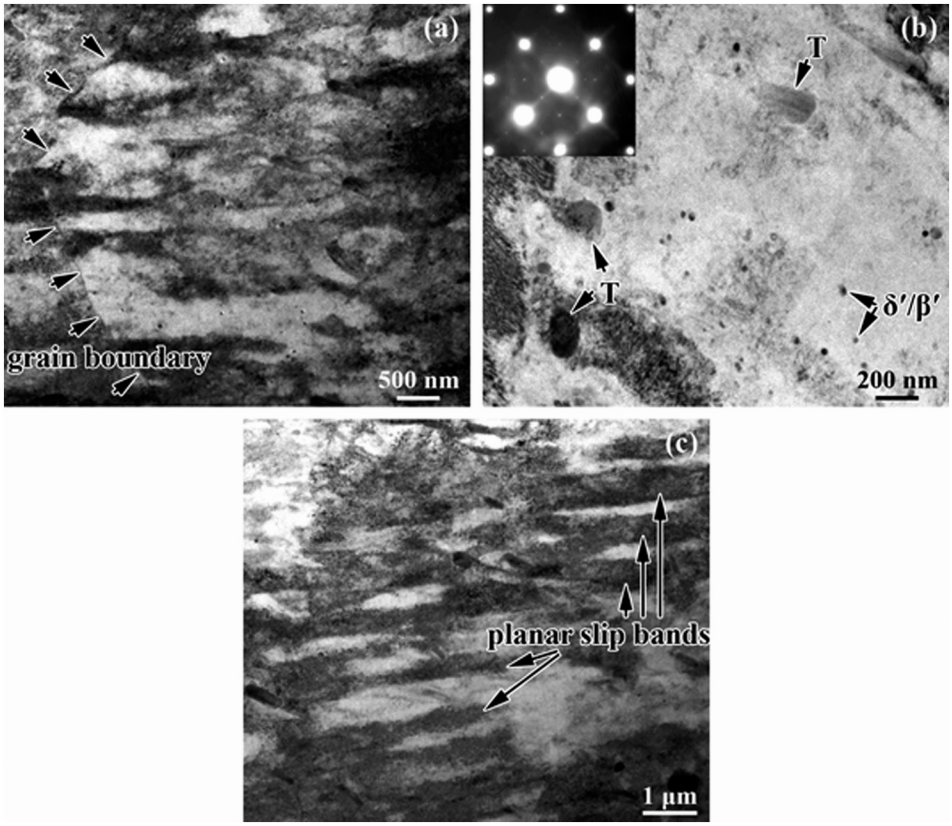

Fig. 10. TEM bright field micrographs of lower TMAZ of failed sample 1200-200: (a) grain structure, (b) precipitates and the SAD pattern in < 100 > zone axis, and (c) dislocation structure.

4.2. Normal fracture behavior of FSW 2060–T8 joints

As mentioned in Part I, the delamination cracking strengthened the TMAZ and HAZ of the FSW 2060–T8 joints. Considering the fact that the LHZs of sample 400–200 was located at the NZ, the hardness of which was only slightly lower than that of the TMAZ and HAZ, sample 400–200 thereby normally fractured at the NZ during tension (Fig. 3e).

Decreasing the welding speed from 200 to 50 mm/min under a constant rotation rate of 1200 rpm led to a sharp decrease of hardness at the LHZs (HAZ) and therefore enlarged the hardness gap between the TMAZ and LHZs for sample 1200–50 (Fig. 2d). The weakening role of δ′/β′ precipitates and soft crystallographic orientation was insufficient to make the TMAZ to be the weakest zone for sample 1200–50, which therefore fractured along the LHZs during tension (Fig. 3h).

5. Conclusions

In order to elucidate the reason for the abnormal failure in the TMAZ rather than the LHZ (HAZ) under 800–200 and 1200 rpm–200 mm/min of FSW 2060-T8 joints, the microstructure and microtexture in the TMAZ and LHZ, as well as the fracture feature in the TMAZ, were investigated in detail. The conclusions are drawn as follows:

(1) Both the LHZ and the upper TMAZ was characterized by elongated lath–shaped grains and ⟨111⟩ crystallographic texture. However, coarse blocky-shaped grains and random crystallographic orientation were detected in the lower TMAZ.
(2) The lower TMAZ exhibited the larger Schmid factor compared with the upper TMAZ and the LHZ, implying that plastic deformation should take place preferentially in the lower TMAZ during tension.
(3) Both coarse grains and δ′/β′ precipitates contributed to the remarkable planar slip in the lower TMAZ during tension, resulting in the local stress concentration at the grain boundaries and weakening the mechanical properties of the lower TMAZ.
(4) Three factors mentioned above, i.e., large Schmid factor, δ′/β′ precipitates and coarse grains were responsible for the abnormal fracture at the TMAZ, with the transgranular fracture in the upper part, but transgranular and intergranular fracture in the lower part.

Data availability

The raw/processed data required to reproduce these findings cannot be shared at this time as the data also forms part of an ongoing study.

Declaration of competing interest

The authors declare that they have no known competing financial interests or personal relationships that could have appeared to influence the work reported in this paper.

Acknowledgements

The authors gratefully acknowledge the support of the National Natural Science Foundation of China (No. U1760201).

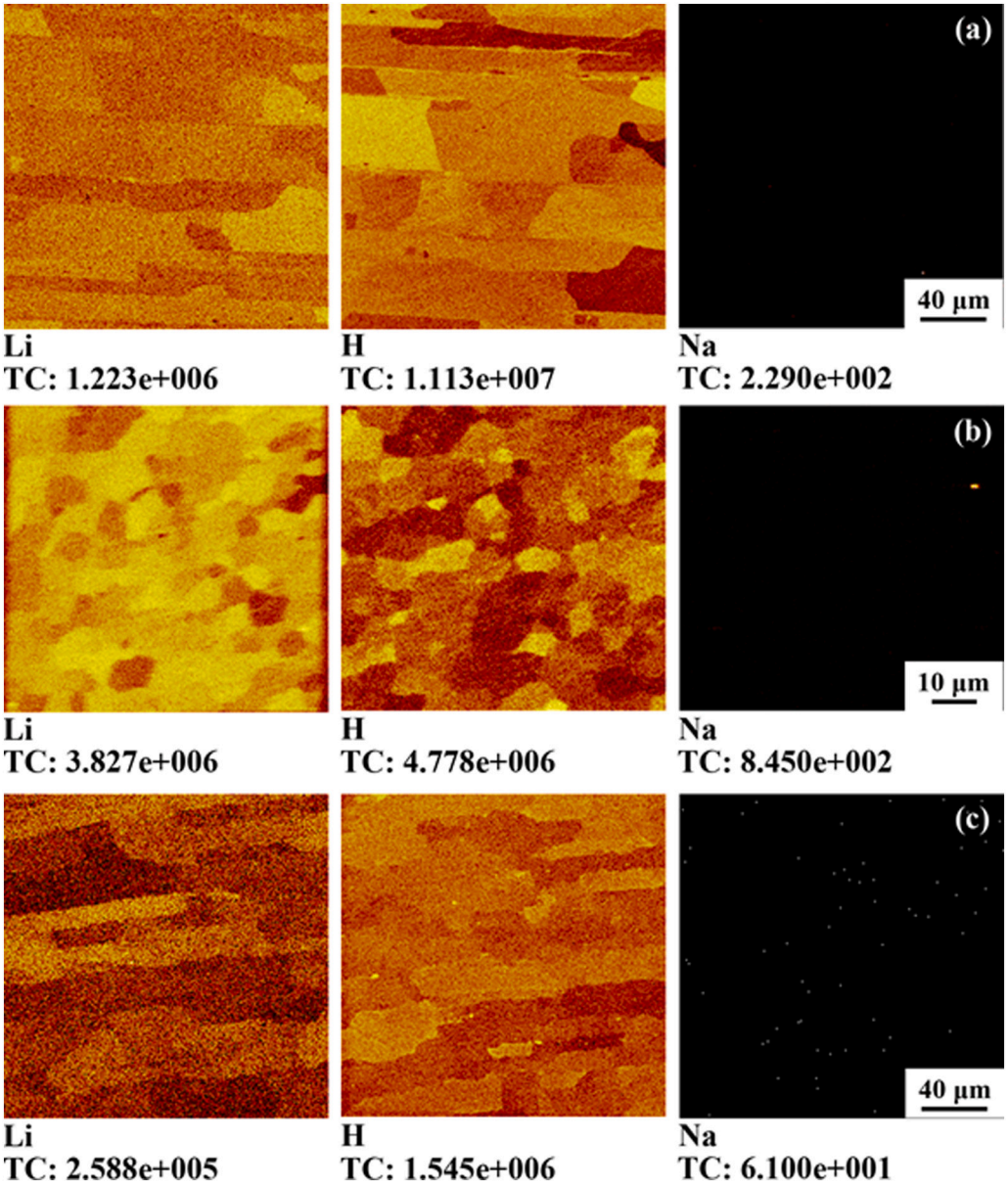

Fig. 11. TOF-SIMS mapping of solute distribution of sample 1200-200: (a) BM, (b) NZ, and (c) lower TMAZ.

References

[1] Y.L. Ma, H.B. Xu, Z.Y. Liang, L. Liu, Corrosion resistance of friction stir welded Al–Cu–Li alloy AA2099-T8, Acta Metal. Sin. (Eng. Lett.) 33 (2020) 127–134, https://doi.org/10.1007/s40195-019-00944-w.

[2] R.J. Rioja, J. Liu, The evolution of Al-Li base products for aerospace and space applications, Metall. Mater. Trans. A 43 (2012) 3325–3337, https://doi.org/10.1007/s11661-012-1155-z.

[3] M.P. Alam, A.N. Sinha, Fabrication of third generation Al–Li alloy by friction stir welding: a review, Indian Acad. Sci. 44 (2019) 153–165, https://doi.org/10.1007/s12046-019-1139-4.

[4] A.A. El–Aty, Y. Xu, X.Z. Guo, S.H. Zhang, Y. Ma, D.Y. Chen, Strengthening mechanisms, deformation behavior, and anisotropic mechanical properties of Al–Li alloys: a review, J. Adv. Res. 10 (2018) 49–67, https://doi.org/10.1016/j.jare.2017.12.004.

[5] Y. Tao, Z. Zhang, D.R. Ni, B.L. Xiao, B.L. Xiao, Z.Y. Ma, Friction stir welding of 2060–T8 Al–Li alloy. Part I: microstructure evolution mechanism and mechanical properties, Mater. Charact. xx (2020) xx.

[6] R.S. Mishra, Z.Y. Ma, Friction stir welding and processing, Mater. Sci. Eng. R 50 (2005) 1–78, https://doi.org/10.1016/j.mser.2005.07.001.

[7] Z.Y. Ma, A.H. Feng, D.L. Chen, J. Shen, Recent advances in friction stir welding/processing of aluminum alloys: microstructural evolution and mechanical properties, Crit. Rev. Solid State 43 (2018) 269–333, https://doi.org/10.1080/10408436.2017.1358145.

[8] Z. Zhang, B.L. Xiao, Z.Y. Ma, Hardness recovery mechanism in the heat–affected zone during long–term natural aging and its influence on the mechanical properties and fracture behavior of friction stir welded 2024Al–T351 joints, Acta Mater. 73 (2014) 227–239, https://doi.org/10.1016/j.actamat.2014.04.021.

[9] A.K. Shukla, W.A. Baeslack, Study of process/structure/property relationships in friction stir welded thin sheet Al–Cu–Li alloy, Sci. Technol. Weld. Join. 14 (2009) 376–387, https://doi.org/10.1179/136217109X412409.

[10] H. Chen, L. Fu, P. Liang, Microstructure, texture and mechanical properties of friction stir welded butt joints of 2A97 Al–Li alloy ultra–thin sheets, J. Alloys Compd. 692 (2017) 155–169, https://doi.org/10.1016/j.jallcom.2016.08.330.

[11] Y. Tao, D.R. Ni, B.L. Xiao, Z.Y. Ma, W. Wu, R.X. Zhang, Y.S. Zeng, Origin of unusual fracture in stirred zone for friction stir welded 2198–T8 Al–Li alloy joints, Mater. Sci. Eng. A 693 (2017) 1–13, https://doi.org/10.1016/j.msea.2017.03.079.

[12] Y.Q. Mao, L.M. Ke, F.C. Liu, C.P. Huang, Y.H. Chen, Q. Liu, Effect of welding parameters on microstructure and mechanical properties of friction stir welded joints of 2060 aluminum lithium alloy, Int. J. Adv. 81 (2015) 1419–1431, https://doi.org/10.1007/s00170-015-7191-2.

[13] B. Cai, Z.Q. Zheng, D.Q. He, S.C. Li, H.P. Li, Friction stir weld of 2060 Al–Cu–Li alloy: microstructure and mechanical properties, J. Alloys Compd. 649 (2015) 19–27, https://doi.org/10.1016/j.jallcom.2015.02.124.

[14] H.J. Liu, Y.J. Hu, C. Dou, D.P. Sekulic, An effect of the rotation speed on microstructure and mechanical properties of the friction stir welded 2060–T8 Al–Li alloy, Mater. Charact. 123 (2017) 9–19, https://doi.org/10.1016/j.matchar.2016.11.011.

[15] K. Yan, T.Y. Wang, H.M. Liang, Y. Zhao, Effects of rotation speed on microstructure and mechanical properties of 2060 Al–Cu–Li alloy in friction stir welding, Mater. Eng. Perform. 27 (2018) 5803–5814, https://doi.org/10.1007/s11665-018-3650-x.

[16] L. Ma, S.Y. Niu, S.D. Ji, P. Gong, Comparative study of 2060-T8 Al-Li alloy friction stir welded joints between natural cooling and water cooling, Arch. Metall. Mater. 65 (2020) 307–314.
[17] Z. Zhang, B.L. Xiao, Z.Y. Ma, Effect of segregation of secondary phase particles and "S" line on tensile fracture behavior of friction stir welded 2024Al-T351 joints, Metall. Mater. Trans. A 44 (2013) 4081–4097, https://doi.org/10.1007/s11661-013-1778-8.
[18] Z. Zhang, B.L. Xiao, Z.Y. Ma, Enhancing mechanical properties of friction stir welded 2219Al–T6 joints at high welding speed through water cooling and post–-welding artificial ageing, Mater. Charact. 106 (2015) 255–265, https://doi.org/10.1016/j.matchar.2015.06.003.
[19] Z. Zhang, B.L. Xiao, Z.Y. Ma, Effect of welding parameters on microstructure and mechanical properties of friction stir welded 2219Al–T6 joints, J. Mater. Sci. 47 (2012) 4075–4086, https://doi.org/10.1007/s10853-012-6261-1.
[20] J. Han, H.J. Li, Z.X. Zhu, F. Barbaro, L.Z. Jiang, H.G. Xu, L. Ma, Microstructure and mechanical properties of friction stir welded 18Cr–2Mo ferritic stainless steel thick plate, Mater. Des. 63 (2014) 238–246, https://doi.org/10.1016/j.matdes.2014.05.070.
[21] L. Zhen, Y.X. Cui, W.Z. Shao, D.Z. Yang, Deformation and fracture behavior of a RSP Al–Li alloy, Mater. Sci. Eng. A 336 (2002) 135–142, https://doi.org/10.1016/S0921-5093(01)01978-5.
[22] A.A. Csontos, E.A. Starke, The effect of inhomogeneous plastic deformation on the ductility and fracture behavior of age hardenable aluminum alloys, Int. J. Plast. 21 (2005) 1097–1118, https://doi.org/10.1016/j.ijplas.2004.03.003.
[23] K.S. Sohn, S.H. Lee, N.J. Kim, In situ observation of microfracture processes in an 8090 Al–Li alloy plate, Mater. Sci. Eng. A 163 (1993) 11–21, https://doi.org/10.1016/0921-5093(93)90573-W.
[24] S.M. Xu, X.M. Deng, A study of texture patterns in friction stir welds, Acta Mater. 56 (2008) 1326–1341, https://doi.org/10.1016/j.actamat.2007.11.016.
[25] E.D. Sweet, S.P. Lynch, C.G. Bennett, R.B. Nethercott, I. Musulin, Effects of alkali–metal impurities on fracture toughness of 2090 Al–Li–Cu extrusions, Metall. Mater. Trans. A 27 (1996) 3530–3541, https://doi.org/10.1007/BF02595445.
[26] S.P. Lynch, Fracture of 8090 Al–Li plate I. Short transverse fracture toughness, Mater. Sci. Eng. A 136 (1991) 25–43, https://doi.org/10.1016/0921-5093(91)90439-T.
[27] S.P. Lynch, B.C. Muddle, T. Pasang, Ductile–to–brittle fracture transitions in 8090 Al–Li alloys, Acta Mater. 49 (2001) 2863–2874, https://doi.org/10.1016/S1359-6454(01)00217-8.
[28] S.P. Lynch, A.R. Wilson, R.T. Byrnes, Effects of ageing treatments on resistance to intergranular fracture of 8090 Al–Li alloy plate, Mater. Sci. Eng. A 172 (1993) 79–93, https://doi.org/10.1016/0921-5093(93)90428-H.